PCCP

PAPER

View Article Online
View Journal

Cite this: DOI: 10.1039/c9cp02891a

Unusual triplet–triplet annihilation in a 3D copper(I) chloride coordination polymer†

Adrien Schlachter,[a] Antoine Bonnot,[a] Daniel Fortin,[a] Paul-Ludovic Karsenti,[a] Michael Knorr[b] and Pierre D. Harvey*[a]

A new coordination polymer (CP) defined as $[Cu_2Cl_2(EtS(CH_2)_4SEt)_4]_n$ (**CP2**) was prepared by reacting $EtS(CH_2)_4SEt$ with CuCl in acetonitrile in a 1 : 2 stoichiometric ratio. The X-ray structure reveals formation of non-porous 3D material composed of parallel 2D-$[Cu_2Cl_2S_2]_n$ layers of Cl-bridged $Cu_2(\mu\text{-}Cl)_2$ rhomboids assembled by $EtS(CH_2)_4SEt$ ligands. A weak triplet emission ($\Phi_e < 0.0001$) is observed in the 400–500 nm range with τ_e of 0.93 (298 K) and 3.5 ns (77 K) as major components. **CP2** is the only 2nd example of emissive thioether/CuCl-containing material and combined DFT/TDDFT computations suggest the presence of lowest energy M/XLCT excited states. Upon increasing the photon flux (*i.e.* laser power), a triplet–triplet annihilation (TTA) is induced with quenching time constants of 72 ps ($k_Q = 1.3 \times 10^{10}$ s^{-1}) and 1.0 ns ($k_Q = 7.1 \times 10^8$ s^{-1}) at 298 and 77 K, respectively, proceeding through an excitation energy migration operating *via* a Dexter process. Two distinct $(I_o)^{1/2}$ (I_o = laser power) dependences of the emission intensity are depicted, indicating saturation as the observed emission increases with the excitation flux. These findings differ from that previously reported isomorphous CP $[Cu_2Br_2(\mu\text{-}EtS(CH_2)_4SEt)_4]_n$ (**CP1**), which exhibits no TTA behaviour at 77 K, and only one (laser power)^2 dependence at 298 K. The ~18-fold increase in k_Q upon warming **CP2** from 77 to 298 K indicates a temperature-aided TTA process. The significant difference between the presence (slower, **CP2**) and absence (**CP1**) of TTA at 77 K is explained by the larger unit cell contraction of the former upon cooling. This is noticeable by the larger change in inter-rhomboid Cu···Cu separation for **CP2**.

Received 21st May 2019,
Accepted 9th July 2019

DOI: 10.1039/c9cp02891a

rsc.li/pccp

Introduction

Triplet–triplet annihilation (TTA) is an important photophysical process that attracts substantial attention nowadays in the fields of materials including metal–organic frameworks (MOFs),[1,2] bio- and therapeutic materials,[3–5] solar cells,[6–8] and organic light emitting devices.[9] Organic polymeric materials are also prone for TTA processes,[10–16] as well as some coordination polymers (CPs).[2,17] In all cases, these materials invariably bear organic chromophores (*i.e.* containing an extended π-system) as the photo-active species. Recently, a large interest for CPs and related hybrids built upon copper(I) halide salts and dithioethers was noticed throughout the literature.[18] Indeed, CPs exhibiting thermal-[19] and vapor-chromisms,[20] redox properties,[21] and anti-proliferative activity[22] were reported, but the major feature is their quasi-omnipresent luminescence behavior,[23–29] including white light emission.[30] Numerous 2-D[31] and 3-D[32] CPs were also reported, including emissive porous[33,34] and semi-porous networks.[35,36] Recently, our groups reported the first CPs (containing any d-block transition metal and any non-chromophoric ligand) exhibiting a TTA process at 298 K for the 3D-$[(Cu_2Br_2)\{\mu\text{-}EtS(CH_2)_4SEt\}]_n$ CP (**CP1**, λ_{emi} = 430 nm, τ_e = 3.4 ns; Cu_2Br_2 exhibits a rhomboid structure).[37] The drastic paucity of examples stems from the lack of favourable structures for triplet energy migration, which mainly relies on the Dexter mechanism[38] (double electron exchange).[39–42] The necessary T_1 energy migration for the TTA process in **CP1** stems from a S-bridged $(Cu_2Br_2)_n$ layer securing connectivity between the rhomboids, therefore the favourable orbital overlaps for the Dexter processes (through bond). So far, there is no evidence for a Förster process (through space).[43] Curiously, the TTA process in **CP1** does not operate at 77 K, which is counter-intuitive since upon cooling lattice contraction, orbital overlaps should increase. Because TTA processes in CPs exhibiting no chromophoric organic ligands are extremely rare, and to shed light on this unexpected lack of TTA behavior at 77 K in **CP1**, the obvious direction to seek answers is the case where X = Cl. However, emissive CPs built upon CuCl/thioether are extremely rare,[31,32] where only one example has been reported so far,[44]

[a] *Département de chimie, Université de Sherbrooke, Sherbrooke, Québec, J1K 2R1, Canada. E-mail: Pierre.Harvey@USherbrooke.ca*

[b] *Institut UTINAM UMR CNRS 6213, Université Bourgogne Franche-Comté, 25030 Besançon, France. E-mail: michael.knorr@univ-fcomte.fr*

† Electronic supplementary information (ESI) available: Complete detail of the DFT and TDDFT computations of **CP2**. CCDC 1886279–1886287. For ESI and crystallographic data in CIF or other electronic format see DOI: 10.1039/c9cp02891a

meaning that luminescence from such material is generally weak. We now report an emissive 3D-$[(Cu_2Cl_2)\{\mu\text{-}EtS(CH_2)_4SEt\}]_n$ CP featuring $Cu(\mu_2\text{-}Cl)_2Cu$ rhomboids (**CP2**) as secondary building units (SBUs), which also exhibits TTA processes at 298 (fast) and 77 K (slow), meaning that the process is temperature-aided. The presence of TTA for **CP2** and not **CP1** at 77 K is due to a larger contraction of the unit cell.

Experimental section

Material

All materials were purchased from Sigma-Aldrich and used without any further purification.

Synthesis of ligand $EtS(CH_2)_4SEt$ (**L**) was adapted from a procedure reported by Hartley *et al.*[45] In a flame dried 250 mL round bottom flask under stirring, sodium (1.0 g, 43.5 mmol) was dissolved in 110 mL absolute ethanol under an argon atmosphere. Ethanethiol (3.2 mL, 43.5 mmol) was added and the solution was stirred for 30 min, and after the solution was refluxed. At this point, 1,4-dibromobutane (2.6 mL, 21.7 mmol) was added dropwise and a white precipitate appeared. The mixture was refluxed for one additional hour and filtered while still hot. Ethanol was removed under reduced pressure. The remaining oil was washed with water and extracted with CH_2Cl_2. The oily residue was dissolved in hot ethanol and stored at 5 °C in a refrigerator. White needles were recovered after one day. 3.0 g, 78%. NMR ^1H δ (ppm) 1.24 (t, 6H), 1.68 (m, 4H), 2.54 (m, 8 H). RMN ^{13}C δ (ppm) 14.91, 26.01, 28.80, 31.31.

Preparation of **CP2** was adapted from a procedure reported by Bonnot *et al.*[37] In a Schlenk tube, CuCl (200 mg, 2.0 mmol) was dissolved in degassed MeCN (10 mL) and **L** (375 mg, 2.1 mmol) was added. After stirring for 1 h, the green solution was stored for one day in a refrigerator at 5 °C. Pale yellow crystals of **CP2** were formed progressively and separated after two days by filtration. Yield (66%). Anal. calc. for C_4H_9ClCuS (188.18): %C 25.53, %H 4.82, %S 17.04; found %C 25.28, %H 4.96, %S 16.86.

Instrumentation

The NMR spectra were recorded on a Bruker Avance 300 Ultrashield NMR spectrometer. The chemical shifts are given in ppm relative to the residual peaks of $CDCl_3$. The thermal analysis (TGA) traces were measured on a PerkinElmer TGA 7 apparatus in the temperature range between 25 and 950 °C at a scanning rate of 10 °C min^{-1} under an argon atmosphere. The solid-state UV-visible spectra were recorded on a Varian Cary 300 Bio UV-vis spectrophotometer at 298 K using grazing-angle transmittance apparatus and a homemade 77 K sample-holder. Samples were dispersed between two quartz plates. Solid-State emission, excitation, lifetimes were acquired on a phosphorimeter FLS980 from Edinburgh Instruments equipped with single monochromators. Samples were introduced in a capillary and spectra obtained were corrected for instrument response. The emission lifetime measurements were performed using a nano-LED laser (λ_{exc} = 378 nm, 5 mW, fwhm = 90 ps). The lifetimes were obtained using a time correlated single photon counting (TCSPC) system and the data were treated from both deconvolution by a multi-exponential analysis and by the exponential series method (ESM). The samples for powder XRD measurements were mixed with a small amount of paratone oil, cut to approximately 0.3 × 0.3 × 0.3 mm^3, and placed on a sample holder mounted at 173.2 K on a Bruker APEX DUO X-ray diffractometer. Six correlated runs per sample with Phi Scan of 360 degrees and exposure times of 270 s were collected with the Cu micro-focus anode (1.54184 Å) and the CCD APEX II detector at a 150 mm distance. These runs, from −12 to −72° 2θ and 6 to 36ω, were then treated and integrated with the XRW2 Eval Bruker software to produce WAXD diffraction patterns from 2.5 to 82° 2θ. The patterns were treated with Diffrac.Eva version 2.0 from Bruker.

Single crystal X-ray

A needle-like specimen of C_4H_9ClCuS, of approximate dimensions 0.040 mm × 0.100 mm × 0.330 mm, was used for the X-ray crystallographic analysis. The X-ray intensity data were measured on a Bruker Kappa APEX II DUO CCD system equipped with a TRIUMPH curved-crystal monochromator and a Mo fine-focus tube (λ = 0.71073 Å). Data collections have been carried out at nine different temperatures – 100, 118, 137, 151, 168, 184, 217, 250 and 298 K using the same crystal. The lattice parameters were obtained by least-squares fit to the optimized setting angles of the entire set of collected reflections. Intensity data were recorded as ϕ and ω scans with κ offsets. No significant intensity decay or temperature drift was observed during data collections. Data were reduced by using DENZO software without applying absorption corrections; the missing absorption corrections were partially compensated by the data scaling procedure in the data reduction. The structure was solved by direct methods with SIR92 program of Altomare *et al.* Refinements were carried out by full-matrix least-squares on F^2 using SHELXL-97 program on the complete set of reflections.[46] All non-hydrogen atoms were refined with anisotropic thermal parameters, whereas the H atoms were treated using a riding model.

Fast kinetic emission decay measurements

The laser source was the SHG of a Solstice (Spectra Physics) Ti–sapphire laser (λ_{exc} = 398 nm; FWHM = 75–100 ps; pulse energy = 0.1 μJ per pulse, rep. rate = 1 kHz; spot size ∼500 μm). The IRF became of a HWHM of 8 ps after passing through the optics. The detector was a Streak Camera (Axis-TRS, Axis Photonique Inc.) with typically less than 8 ps resolution. Samples were dispersed between two quartz plates. The results were also globally analysed with the program Glotaran (http://glotaran.org) permitting to extract a sum of independent exponentials: $I_{(\lambda,t)} = C_1(\lambda) \times \exp(-t/\tau_1) + C_2(\lambda) \times \exp(-t/\tau_2) + \ldots$. The experiments using high laser power were performed to the limit of the thermal (or photochemical) stability of the samples. This stability was verified by measuring the powder X-ray diffraction patterns.

Computations

All density functional theory (DFT) and time-dependant (TD-DFT) calculations were performed with Gaussian 16[47] at the

Université de Sherbrooke with the Mammouth supercomputer supported by Le Réseau Québécois De Calculs Hautes Performances. The .cif file from DRX structures has been used as optimized structure for calculations. The DFT (singlet and triplet energy states) as well as TD-DFT[48–57] calculations were carried out using the B3LYP method. VDZ (valence double ζ) with SBKJC effective core potentials were used for all Cu and Br atoms[58–63] and 3-21g* basis set was used for C, H and S atoms.[57] The calculated absorption spectra were obtained from GaussSum 3.0.[64]

Results and discussion

Synthesis and characterization

CP2 was prepared by reacting 1,4-bis(ethylthio)butane with CuCl in acetonitrile. Pale yellow air-stable crystals suitable for X-ray structure determination grew upon standing (see ESI† for the crystal data). The X-ray data of this material, which is isostructural with **CP1** (monoclinic, space group $P2_1/n$), reveal the presence of a non-porous 3D CP (Fig. 1) built upon parallel 2D-$[Cu_2Cl_2S_2]_n$ layers (Fig. 1b) of S-bridged Cu_2Cl_2 rhomboids. Noteworthy, in contrast with most dithioether-assembled CPs incorporating $Cu(\mu_2\text{-}X)_2Cu$ SBUs, the rhomboids within the layers are linked in a Cu ← S → Cu mode, *i.e.* a S-atom acts as a 4-electron donor implying a dative bonding using all two non-bonding doublets. The very loose Cu···Cu contact of >3.29 Å (Table S3, ESI†) excludes any intermetallic interactions and exceeds those for other CPs such as 1D $[\{Cu(\mu_2\text{-}Cl)_2Cu\}(\mu_2\text{-medithiane})_2]_n$ (3.0517(8) Å) or 2D $[\{Cu(\mu_2\text{-}Cl)_2Cu\}(\mu_2\text{-}sec\text{-budithiane})_2]_n$ (2.8715(9) Å).[65] These layers are held together by $EtS(CH_2)_4SEt$ assembling ligands below and above these planes (Fig. 1c). The $Cu_2Cl_2S_4$ rhomboids are centrosymmetric (Fig. 1a), but the Cu–Cl and Cu–S bond lengths differ by ~0.08 and ~0.05 Å, respectively, at 298 K. No phase-transition was noticed in the temperature range from 100 to 298 K.

The thermal stability was addressed by TGA (Fig. 2). The traces are characterized by a first weight loss starting at ~175 °C and stopping at ~230 °C to form a plateau with a weight loss of 49.2%. Then, another weight loss starts near 400 °C and spreads all the way to 890 °C. The remainder accounts for 11.3% of residual materials. This well-defined TGA trace cannot straightforwardly be interpreted by sequential ligand losses (*i.e.* $EtSC_4H_8SEt$ (−47.4%), then Cl_2 (−18.8%), with "Cu_2" (−33.8%) as residual; Table 1). Instead, the weight losses are better explained by a decomposition of the dithioether where one Et group remains in the solid (presumably captured by a Cu atom) in exchange of one Cl atom. Then, volatile organo-copper species are generated in the large 400–890 °C range. The residual is most likely pure copper based on its characteristic colour.

Photophysical properties

Prior to measurements on powder samples, the PXRD patterns were systematically compared to the calculated one issued from the single crystal X-ray data and the match was excellent in all cases (Fig. 3, bottom).

The absorption, excitation and emission spectra of **CP2** at 298 and 77 K are presented in Fig. 3 (top). The absorption spectra are characterized by two maxima: ~270 and ~330 nm. The interpretation of these bands has been made with the help of DFT and TDDFT computations. The preparation of the input file was executed by taking a CP fragment composed of 8 Cu_2Cl_2 rhomboid units directly extracted from the X-ray data and the peripheral uncoordinated Cu atoms were then saturated by EtSEt groups. These capping ligands were then optimized while the central X-ray structure was non-optimized. The resulting representations of the frontier MOs are provided for both the

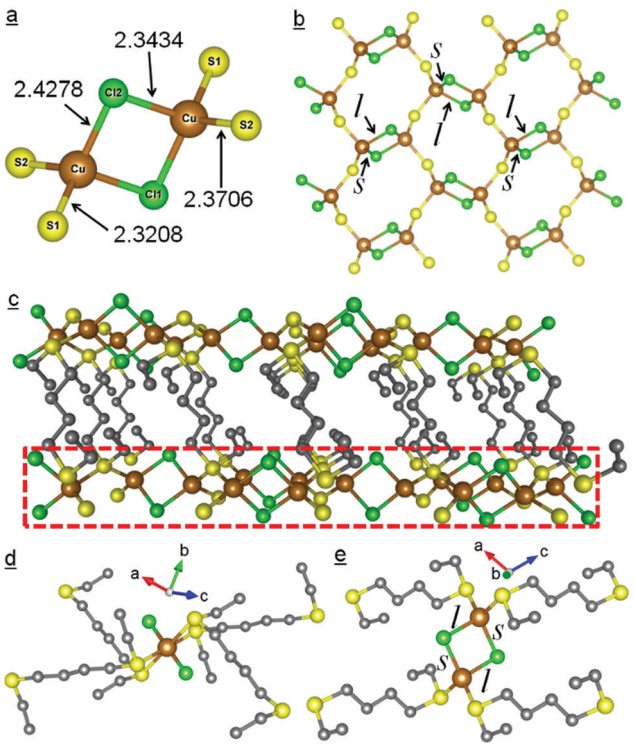

Fig. 1 (a) One $Cu_2Cl_2S_4$ rhomboid unit with bond distances (298 K, see the ESI† for the uncertainties or Fig. 9 below). (b) Top view of a $[Cu_2Cl_2S_2]_n$ layer (s = short; l = long). (c) Side view of the 3D **CP2** (the rectangle shows a $[Cu_2Cl_2S_2]_n$ layer). (d) and (e) Representations of one $Cu_2Cl_2(EtS(CH_2)_4SEt)_4$ unit along the *a*, *b* and *c* axes.

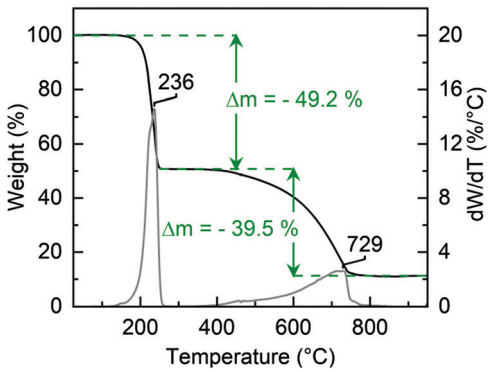

Fig. 2 TGA trace (black) and its first derivative (grey) of **CP2** under Ar atmosphere in the range of 25 to 950 °C. Scan rate = 10 °C min^{-1}.

Table 1 TGA data for **CP2**

$[(Cu_2Cl_2)EtSC_4H_8SEt]_n$ M = 376.32 g mol^{-1} (n = 1)	T range (°C)	$^{Exp.}\Delta m$ (%)	$^{Calc.}\Delta m$ (%)	Proposed assignment
	175–230	−49.2	−49.1	$EtSC_4H_8S$ + Cl
	400–890	−39.5	−39.6	2/3Cu + Et + Cl
	890–950	−11.3	−11.3	1/3Cu

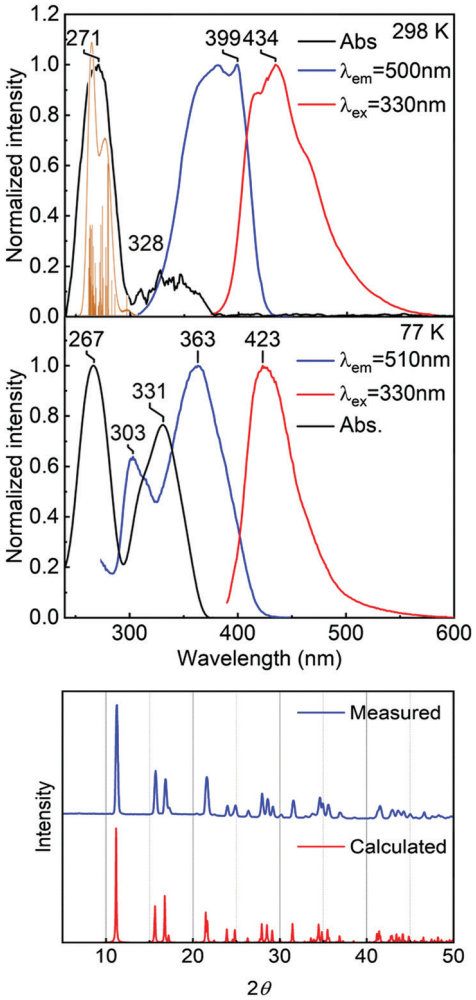

Fig. 3 Top: Absorption (black), excitation (blue) and emission (red) spectra of **CP2** at 298 and 77 K. The orange bars represent the calculated positions of the spin-allowed transitions ($S_0 \rightarrow S_n$) of **CP2** by TDDFT (described below). See Fig. 5 below for a larger scale. The orange curve is generated by assigning and arbitrary thickness of 500 cm^{-1} to each transition. Bottom. Calculated (red) and experimental (blue) powder X-ray diffraction patterns at 173 K for 2θ ranging from 5° to 50° for **CP2**. The calculated and measured diffraction patterns match well, confirming the homogeneity of the crystalline phases.

singlet and triplet states (Fig. 4) along with the calculated atomic contributions separated in Cu, Cl and thioether fragments (Table 2). By examining the change in these relative atomic contributions upon the HOMO → LUMO (singlet) and LSOMO → HSOMO (triplet) transitions, these computations predict that charge transfer excited states of the type (Cu_2Cl_2)-to-SRR' are generated, often referred as M/XLCT.

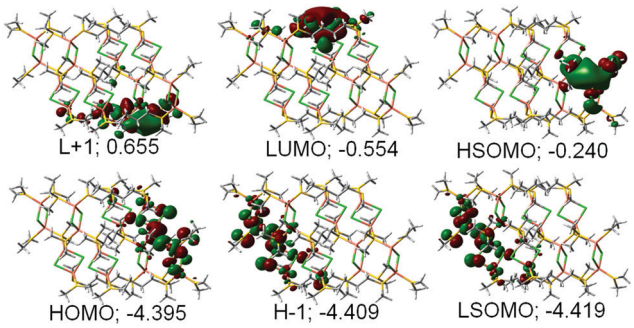

Fig. 4 Representation of selected frontier MOs for **CP2** for the singlet state, H = HOMO, L = LUMO (see ESI† for more MOs); for the triplet state, LSOMO and HSOMO are the lowest and highest semi-occupied molecular orbitals, respectively. The energies are in eV.

Table 2 Calculated atomic contributions (in %) of the frontier MOs for various fragments of **CP2**; LS = LSOMO, HS = HSOMO

	HOMO−1	HOMO	LUMO	LUMO+1
Ligand	33.7	32.0	61.5	47.9
Cu	50.6	51.7	37.6	51.3
Cl	15.7	16.3	0.9	0.9
	LS−1	LS	HS	HS+1
Ligand	37.7	34.0	60.1	61.3
Cu	49.2	50.3	33.3	37.9
Cl	13.1	15.7	6.6	0.8

Using TDDFT, the positions and oscillator strength (f) of the first 50 spin-allowed (*i.e.* $S_0 \rightarrow S_n$; $n > 0$) electronic transitions were computed (detail placed in the ESI†). A bar graph reporting the positions and the oscillator strength for each transition is provided in Fig. 5. The bulk of these transitions are placed in the 260–280 nm window. By assigning an arbitrary thickness of 500 cm^{-1} to each transition, a simulated spectrum is generated (see solid line). The comparison of the bar graph and simulated spectrum with the experimental data (see orange trace in Fig. 3, top) is excellent and match perfectly the feature located at ~270 nm. This result permits to assign the remaining feature at ~ 330 nm to spin-forbidden transitions (*i.e.* $S_0 \rightarrow T_n$; $n > 0$).

Emission properties

CP2 is weakly emissive at both 298 and 77 K (Fig. 3, red traces). This feature is in itself very rare as the only other example of a thioether-based CuCl-containing material is the 2D-CP of formula $[(CuCl)(BzSCH_2C{\equiv}CCH_2SBz)]_n$ composed of polycyclic $[Cu_6Cl_6{=}Cu_6Cl_6{=}]_n$ ribbons cross-linked by $BzSCH_2C{\equiv}CCH_2SBz$ ligands.[44] The emission quantum yield (Φ_e, at 298 K) of **CP2** is very low (*i.e.* below the detection limit of the integration sphere). Few remarks are worthy. First, this observation is simply consistent with the fact that emissive CuCl/thioether-containing species are extremely rare, meaning that the paucity of examples is readily due to intrinsic very low emission quantum yields in such materials. Second, the position of the emission band (*i.e.* in the 400–500 nm window, with a maximum in the vicinity of 420–435 nm) is in line with what is generally reported for the often more emissive

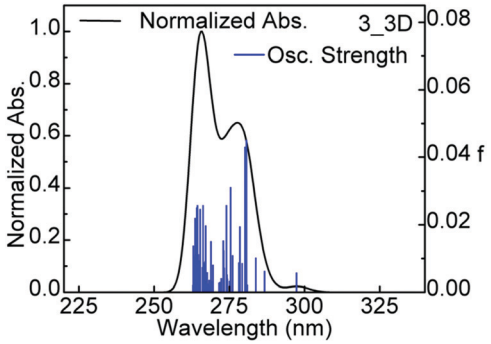

Fig. 5 Representation of 50st electronic transitions calculated by TDDFT of a fragment of **CP2** (bar graph; f = computed oscillator strength). The black line is generated by assigning a thickness of 500 cm^{-1} to each bar. (H = HOMO, L = LUMO).

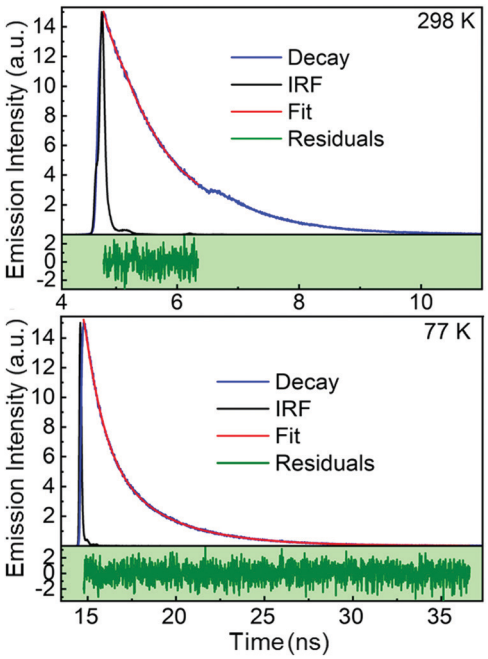

Fig. 6 Emission decays of **CP2** (blue), fit (red), IRF (black) and residual (green) using a nano-LED laser (λ_{exc} = 378 nm; fwhm = 90 ps; power = 0.45 pJ) at 298 K (τ_{e1} {f%} = "0.03" ns {3.0}; τ_{e2} {f} = 0.93 ns {97.0}, χ^2 = 1.16) and 77 K (τ_{e1} {f%} = 1.0 ns {32.6}; τ_{e2} {f%} = 3.5 ns {67.4}, χ^2 = 1.06). Note that this 0.03 ns value is not considered accurate due pulse width at half-maximum of the excitation source and its relative intensity (see footnote of Table 3).

$Cu_2Br_2S_4$ rhomboid-containing materials (*i.e.* 400 < λ_{em} < 450 nm).[18,66–69] Third, with an expected very low Φ_e value (<0.0001), it is expected that the triplet excited state lifetime (τ_e) will also be short (as observed, see below). The τ_e data is generally encountered for the $Cu_2Br_2S_4$ species are 0.6 < τ_e < 66 μs,[18,66–69] but no Φ_e data are available. For comparison purposes, some strongly emissive $(Cu_2I_2)_m$/thioether species (m = 1, 2, 4) are also known with typical Φ_e values ranging between 0.10 and 0.56, and exhibit τ_e's of 0.2 to 5.2 μs.[36,70] Noteworthy, $Cu_2Br_2S_4$-rhomboid-containing CP's exhibiting τ_e in the short ns time scale are also known.[71] Assuming that one can transfer the radiative (k_r) and non-radiative (k_{nr}) rate constants from CuI- to CuBr- to CuCl-materials, qualitatively a decrease in Φ_e by 3 orders of magnitude should proportionally result in a decrease in τ_e as well (*i.e.* from μs to ns time scale). Experimentally, this is precisely what is observed (Table 3).

The emission decays (Fig. 6) are found bi-exponential (*i.e.* increasing the number of components to the decay analysis did not reveal any significant new components and did not improve the χ^2 significantly; moreover, upon higher laser power two slopes in the log scale graphs were unambiguously observable; see Fig. 8 below). The presence of a TTA process was then suspected ($T_1 + T_1 \rightarrow S_0 + T_n$ + heat; then $T_n \rightarrow T_1$). An investigation of the laser power dependence of the total emission intensity and the relative intensity of both components was undertaken. Indeed, the total emission intensity (I_e) follows a linear trend with the square root of the laser intensity ($I_0^{1/2}$; Fig. 7), thus demonstrating TTA. However, the graphs at both temperatures show two regions (low- and high-power regions), thus indicate the presence of saturation in the high-power region. Indeed, the graphs of I_e *vs.* (I_o) is linear for the high-power region, whereas the low-power one is not (see ESI†). Additionally, the relative intensity of the short components (72 ± 6 ps at 298 K and ~1.0 ns at 77 K; Streak camera) over their long ones (1.03 ns at 298 K and 3.5 ns at 77 K; Streak camera), *i.e.* I_e(short)/I_e(long), increases with the laser flux (Fig. 8; note that the decays are presented in semi-log format for convenience). Conclusively, the short component is the lifetime of the quenched species during the annihilation.

The emission quenching rates upon TTA, k_Q, was evaluated using $k_Q = (1/\tau_e) - (1/\tau_e^{\circ})$[72] where τ_e and τ_e° are respectively the quenched (72 ps (298 K); 1.0 ns (77 K)) and unquenched (1.0 ns (298 K); 3.5 ns (77 K)) components. These k_Q values are 1.3 × 10^{10} (298) and 7.1 × 10^8 (77 K), indicating that the thermal activation plays a role. Noteworthy, the former k_Q value is fast and is precisely in the same order of magnitude to that reported for MOFs (~10^{10} s^{-1}; 298 K),[73] and also compares favourably to that for **CP1**[37] (quenched component, τ_e ~ 100 ps;

Table 3 Photophysical data for **CP2** at minimal light flux

	T (K)	λ_{ex} (nm)	λ_{em} (nm)	fwhm (cm^{-1})	Δ_{fwhm}[a] (cm^{-1})	τ_e[b] (ns)	χ^2	Φ_e[c]	k_r[d] (10^5 s^{-1})	k_{nr}[d] (10^9 s^{-1})
CP2	298	399	434	3600	500	*0.03*, 0.93	1.16	<0.0001	<1	~1.1
	77	363	423	3100		1.02, 3.52	1.06	—	—	—

[a] Δ_{fwhm} = (fwhm 298 K) − (fwhm 77 K); fwhm = full width at half-maximum. [b] TCSPC data (±10%). The 0.03 ns value is not accurate due to its relative intensity (~3%) and fwhm of the laser pulse (90 ps). A more accurate value was measured to be 72 ± 6 ps using a streak camera and fs-laser system (see below). [c] Φ_e: emission quantum yield (detection limit ~10^{-4}) at 298 K. [d] $k_r = \Phi_e/\tau_e$; $k_{nr} = (1 - \Phi_e)/\tau_e$.

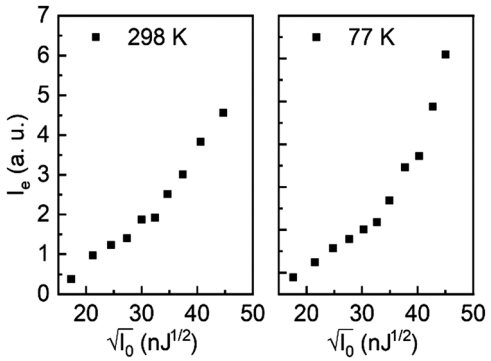

Fig. 7 Graph of I_e *vs.* (laser power)$^{1/2}$. Note that the powder XRD traces before and after submitting the samples to laser irradiation were measured. All samples turned out stable using these laser flux conditions (Fig. 8, bottom). The slopes of the low-power regions are 0.102 (298) and 0.086 (nJ$^{1/2}$)$^{-1}$ (77 K), which is consistent with the slower excitons (and k_Q values) at low temperature (see text).

unquenched component = 3.45 ns; *i.e.* $k_Q \sim 0.97 \times 10^{10}$ s^{-1}). This fast rate may stem from the contribution of two mechanisms; Föorster and Dexter. However, the 77 K rate is significantly slower (for **CP2**) and inexistent for **CP1**. Two new features are observed for **CP2**: presence of a TTA at 77 K, and of two regions in the (laser power)$^{1/2}$ dependence on the emission intensity, here due to saturation, is not observed for **CP1**.

Comparison with the $[Cu_2Br_2(\mu\text{-EtS}(CH_2)_4SEt)_4]_n$ polymer (CP1)

Prior to present the X-ray study *vs.* temperature, a comparison of the key parameters of both CPs is given (Table 4). The key features are as follow: (1) the k_Q values at 298 K are in the order of 10^{10} s^{-1}, (2) at 77 K, the TTA process is either slow (**CP2**) or too slow to be detected (**CP1**), and (3) for a 100 K temperature lowering, the unit cell parameters experience a larger decrease for **CP2** (see detail in the ESI†) than for **CP1** (see detail in the ESI of ref. 37). The k_Q values are, again, linked to the rate of excitation energy migration, k_{hop}. At 298 K, the rates are in the same order of magnitude for **CP1** and **CP2**, which is consistent with their isomorph structures. Upon lowering the temperature, the TTA process either slows down or stops, meaning that the TTA is temperature-aided. However, this process is not completely stopped in **CP2**, which is explained by the larger unit cell contraction upon cooling. In addition, there is no evidence for a two TTA zones (*i.e.* TTA and saturation) in the graph of the emission intensity *vs.* (laser power)^2 for **CP1** at 298 K (as this is the case for **CP2** in Fig. 7). The saturation points where the lines curve between lower and higher laser power zones for **CP2** are ~32 (nJ)$^{1/2}$ (298 K) and ~38 (nJ)$^{1/2}$ (77 K). These values indicate that the migration processes (k_{hop}) are slower at 77 K, which is fully consistent with the trend k_Q (298 K) > k_Q (77 K).

X-ray structure *vs.* temperature and interpretation of the TTA at 77 K (CP1 *vs.* CP2)

Expectedly, the unit cell volume and parameters *a*, *b*, and *c* expand, and the density decreases, with the temperature (ESI†).

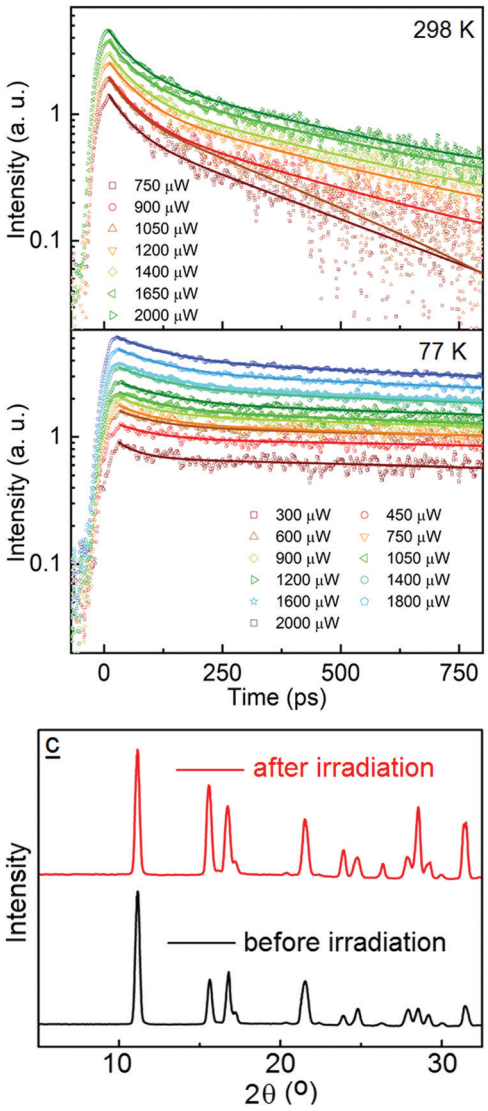

Fig. 8 Top: Semi-log plots of the emission decay traces of **CP2** at 298 and 77 K as a function of laser excitation intensity: I_e(short)/I_e(long) = 1.24 (750), 1.05 (1050), 1.78 (1200), 1.72 (1400), 1.85 (1650), and 1.92 (2000 μW) at 298 K; 0.32 (450), 0.44 (600), 0.55 (750) 0.51 (900), 0.58 (1050), 0.58 (1200), 0.67 (1400) 0.65 (1600), 0.69 (1800), 0.69 (2000 μW). Bottom: Comparison of the experimental powder XRD from 5° to 50° before and after laser irradiation (*i.e.* before and after the measurements). The short (72 ± 6 ps) and long (1.03 ± 0.10 ns) lifetimes at 298 K remain about constant with the power.

Similarly, the Cu–S bond lengths increase with the temperature and the slopes bond length *vs.* temperature, Δd(Cu–S)/ΔT, differ somewhat. Concurrently, the Cu–Cl bonds behaves slightly differently where one bond exhibits a modest positive slope (Δd(Cu–Cl2)/ΔT) while one remains constant (Δd(Cu–Cl1)/ΔT). The reason for this stems from the dissymmetric dilatation of the unit cell parameters with the temperature: +0.026(2), +0.054(2) and +0.043(2) Å, respectively representing relative increases of 0.29, 0.60 and 0.39%, for *a*, *b*, and *c*, from 100 to 298 K (at 100 K, *a* = 8.9309, *b* = 6.7591, *c* = 10.8963 Å). The contraction of the unit cell parameters upon cooling **CP1** and

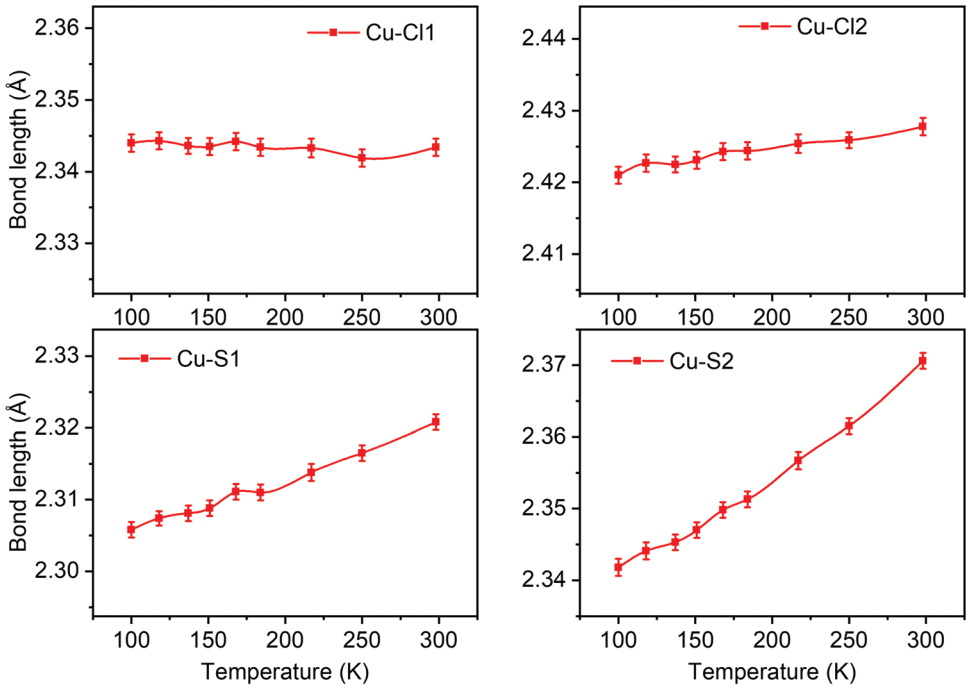

Fig. 9 Graph of the Cu–Cl and Cu–S bond lengths *vs.* temperature. The error bars are the uncertainties and the scalings are set identical for comparison purposes; *i.e.* to stress the fact that the slopes are different. The atom numbering refers to Fig. 1.

Table 4 Comparison between **CP1** and **CP2** (tw = this work)

CP	**CP2** (X = Cl)[tw]		**CP1** (X = Br)[37]		Comment
TGA	T_{dec} > 175 °C		T_{dec} > 211 °C		**CP1** is more therm. stable
T (K)	298	77	298	77	
λ_{exc} (nm)	399	363	367	385	
λ_{em} (nm)	434	423	430	416	Common for rhomboids
τ_e (minor)[a]	*0.03 ns*	1.02 ns	—[b]	—[b]	
τ_e (major)[a]	0.93 ns	3.52 ns	3.45 ns	3.35 ns	Not unusual for rhomboids
Φ[e]	<0.0001	—[d]	<0.0001	—[d]	Not unusual for rhomboids
k_{nr} (10^8 s^{-1})[c]	~11	—[d]	~2.9	—[d]	
TTA	Yes	Yes	Yes	No	Based on linearity of I_e *vs.* $(I_o)^{1/2}$
Quenched comp. (ps)	72	~1000	~100	—[d]	Measured with a streak camera
k_Q (s^{-1})[f]	~10^{10}	~7 × 10^8	~10^{10}	—[d]	10^{10} (298 K) is typical for TTA evidence for thermal activation
Δa (Å)	0.020		0.011		123 < T (K) < 293 for **CP1**
Δb (Å)	0.048		0.027		118 < T (K) < 298 for **CP2**
Δc (Å) for a 170 K range	0.037		0.035		**CP2** contracts more than **CP1** explaining the lack of TTA for **CP1** at 77 K
$d_{(Cu\cdots Cu)}$ at 293 K	3. 2903(10) Å		3.459(10) Å		In the Cu(μ_2-X)$_2$ Cu rhomboids
$\Delta(d_{Cu\cdots Cu})$ for a 170 K range	0.040 (Å)		0.032 (Å)		In the Cu–S–Cu bridges
nb. of TTA mechanisms	2	2	1	0	Presence of exciton saturation or not

[a] TCSPC data at minimal light excitation flux. The 0.03 ns value for **CP2** is not accurate due to its relative intensity (~3%; see caption of Table 3). The short components are the quenched component due to TTA. [b] These short components are not observed at minimal light flux, but at 298 K the quenched component is observed with a value of ~100 ps (Streak camera) with higher excitation power. [c] Note that the larger k_{nr} value for **CP2** is consistent with the observation that emissive Cu–Cl CPs are extremely rare meaning that k_{nr} is large for these species. A lower rigidity of the Cu–Cl framework appears to be responsible for the larger k_{nr}. [d] Not accessible. [e] No TTA process observed. [f] Note that in absolute values not considering the uncertainties k_Q (**CP1**) < k_Q (**CP2**).

CP2 within the same temperature range (here 170 K; Table 4) is larger for **CP2**, meaning that the shrinkage of some separations is more important for the latter. Indeed, the change in inter-rhomboid distance, $\Delta(d_{Cu\cdots Cu})$, is larger for **CP2**, is one example (0.040 *vs.* 0.032 Å).

The slower k_Q value (therefore k_{hop}) for **CP2** and the absence of TTA for **CP1** (or too slow to be observed) at 77 K in comparison with the faster k_Q values at 298 K (10^{10} s^{-1}) indicate that the TTA is temperature-driven. Noteworthy, thermally aided processes are also known for organics. For example, an increase in rate of excitation energy migration and singlet–singlet annihilation with the temperature for liquid benzene was reported over a decade ago.[74] Moreover, **CP1** does not exhibit a TTA, whereas **CP2** does. The X-ray data indicate a larger unit cell contraction for **CP2** for a same temperature range. This larger shrinkage implies a larger decrease in bond

distances and separations for **CP2**, thus promoting better conditions for excitation energy migration.

During the course of this investigation, an unusual structural feature was observed. Indeed, the intra-rhomboid Cu···Cu separation appears to increase (very slightly) from 100 to 170 K, but experiences a clear decrease (0.004 Å) going from 170 to 250 K (ESI†). Considering the uncertainties, this feature is real, again associated with the dissymmetry of the non-cubic 3D geometry (Fig. 1). However, this change is so small (0.004 Å) that it bears no consequence on the interpretation of the TTA processes, but is worth noting.

Finally, attempts were also made to observe an emission from upper states ($T_1 + T_1 \rightarrow S_0 + T_n$ + heat or $S_0 + S_n$ + heat), but stubbornly failed (note that the detection limit is $\sim$250 nm). The reason most likely lies in the density of states located nearby to each other (as well illustrated for the S_n in Fig. 5; it is reasonably assumed that this is also true for the T_n states), thus providing a very large number of non-radiative deactivation paths.

Conclusion

The isomorph **CP1** and **CP2** are still, to the best of our knowledge, the only examples of CPs containing d-block transition metals and non-chromophoric ligands that exhibit TTA processes. The particularity of the earlier work for **CP1** (X = Br) was the absence of TTA at 77 K, whereas at 298 K, the process is fast. The extension of the past work to the case where X = Cl (**CP2**) was natural and helped shining light on this curious result. The faster rate of TTA at 298 K in comparison with that at 77 K indicates that the process is clearly temperature-aided, which can also explain the absence of TTA for **CP1** at 77 K (*i.e.* too slow to be observed). The presence of a slow TTA process for **CP2** and not at all for **CP1** at 77 K, is explained by the significantly larger unit cell contraction upon lowering the temperature to 77 K in **CP2**. The rates of emission quenching by TTA, k_Q, at 298 K (1.3×10^{10} s^{-1} for **CP2** and 0.97×10^{10} s^{-1} for **CP1**) compare favourably to other CPs containing organic ligands (time scale $\sim 10^{10}$ s^{-1}) and are considered fast. This outcome stems from the presence of strong MO couplings between the rhomboid units (through bond) within the 2D-$[Cu_2Cl_2S_2]_n$ layers as deduced by DFT computations. Noteworthy, the duality has been reported before for singlet energy transfer.[75] Finally, the presence of two regions (TTA and saturation) is observed for **CP2** in the graph emission intensity *vs.* (laser power)$^{1/2}$. The fact that the saturation point being is at higher power at 77 K is fully consistent with the slower k_Q values (*i.e.* which is related to k_{hop}) measured for this temperature. All in all, the TTA is a common photophysical event to all CPs and MOFs, regardless of the units that compose these materials. This knowledge is useful for the design of new materials, including with the hope of inducing observable upper energy emissions, or simply converting into heat.

Conflicts of interest

There are no conflicts to declare.

Acknowledgements

This research was supported by the Natural Sciences and Engineering Research Council of Canada (NSERC).

References

1 Y. Zhang, D. Yang, J. Han, J. Zhou, Q. Jin, M. Liu and P. Duan, Circularly Polarized Luminescence from a Pyrene-Cyclodextrin Supra-Dendron, *Langmuir*, 2018, **34**, 5821–5830.
2 R. Medishetty, J. K. Zareba, D. Mayer, M. Samoć and R. A. Fischer, Nonlinear optical properties, upconversion and lasing in metal–organic frameworks, *Chem. Soc. Rev.*, 2017, **46**, 4976–5004.
3 L. Huang, E. Kakadiaris, T. Vaneckova, K. Huang, M. Vaculovicova and G. Han, Designing next generation of photon upconversion: Recent advances in organic triplet–triplet annihilation upconversion nanoparticles, *Biomaterials*, 2019, **201**, 77–86.
4 Q. Dou, L. Jiang, D. Kai, C. Owh and X. J. Loh, Bioimaging and biodetection assisted with TTA-UC materials, *Drug Discovery Today*, 2017, **22**, 1400–1411.
5 M. Scholz and R. Dedic, *Singlet Oxygen: Applications in Biosciences and Nanosciences*, 2016, vol. 2, pp. 63–81.
6 J. Pedrini and A. Monguzzi, Recent advances in the application triplet–triplet annihilation-based photon upconversion systems to solar technologies, *J. Photonics Energy*, 2017, **8**, 1.
7 T. Dilbeck and K. Hanson, Molecular Photon Upconversion Solar Cells Using Multilayer Assemblies: Progress and Prospects, *J. Phys. Chem. Lett.*, 2018, **9**, 5810–5821.
8 Y. Shang, S. Hao, C. Yang and G. Chen, Enhancing Solar Cell Efficiency Using Photon Upconversion Materials, *Nanomaterials*, 2015, **5**, 1782–1809.
9 Q. Wei, N. Fei, A. Islam, T. Lei, L. Hong, R. Peng, X. Fan, L. Chen, P. Gao and Z. Ge, Small-Molecule Emitters with High Quantum Efficiency: Mechanisms, Structures, and Applications in OLED Devices, *Adv. Opt. Mater.*, 2018, **6**, 1800512.
10 M. Aydemir, The contribution of triplet excitons to the total singlet production yield in a sky-blue emitting co-polymer film, *Polym. Bull.*, DOI: 10.1007/s00289-019-02729-8.
11 P. Wang, Q. Huang, S. Zhao, Z. Qin, Z. Xu, D. Song and B. Qiao, Investigating the evolution of excitons in polymer light-emitting diodes by transient measurement, *Org. Electron.*, 2019, **68**, 45–49.
12 A. Dey and D. Kabra, Role of Bimolecular Exciton Kinetics in Controlling the Efficiency of Organic Light-Emitting Diodes, *ACS Appl. Mater. Interfaces*, 2018, **10**, 38287–38293.
13 S. Masoomi-Godarzi, M. Liu, Y. Tachibana, L. Goerigk, K. P. Ghiggino, T. A. Smith and D. J. Jones, Solution-Processable, Solid State Donor–Acceptor Materials for Singlet Fission, *Adv. Energy Mater.*, 2018, **8**, 1801720.
14 N. Chitraningrum, T. Y. Chu, P. T. Huang, T. C. Wen and T. F. Guo, The triplet–triplet annihilation process of triplet to singlet excitons to fluorescence in polymer light-emitting diodes, *Org. Electron.*, 2018, **62**, 505–510.

15 T. Zhang, J. Sun, X. Liao, M. Hou, W. Chen, J. Li, H. Wang and L. Li, Poly(9,9-dioctylfluorene) based hyperbranched copolymers with three balanced emission colors for solution-processable hybrid white polymer light-emitting devices, *Dyes Pigm.*, 2017, **139**, 611–618.
16 R. Andernach, H. Utzat, S. D. Dimitrov, I. McCulloch, M. Heeney, J. R. Durrant and H. Bronstein, Synthesis and exciton dynamics of triplet sensitized conjugated polymers, *J. Am. Chem. Soc.*, 2015, **137**, 10383–10390.
17 M. Hosoyamada, N. Yanai, K. Okumura, T. Uchihashi and N. Kimizuka, Translating MOF chemistry into supramolecular chemistry: Soluble coordination nanofibers showing efficient photon upconversion, *Chem. Commun.*, 2018, **54**, 6828–6831.
18 P. D. Harvey and M. Knorr, Luminescent coordination polymers built upon Cu_4X_4 (X = Br, I) clusters and mono- and dithioethers, *Macromol. Rapid Commun.*, 2010, **31**, 808–826.
19 T. H. Kim, Y. W. Shin, J. H. Jung, J. S. Kim and J. Kim, Crystal-to-crystal transformation between three CuI coordination polymers and structural evidence for luminescence thermochromism, *Angew. Chem., Int. Ed.*, 2008, **47**, 685–688.
20 J. Zhang, M. Li, L. Cheng and T. Li, Multifunctional polymers built on copper–thioether coordination, *Polym. Chem.*, 2017, **8**, 6527–6533.
21 M. Rasouli, M. Morshedi, M. Amirnasr, A. M. Z. Slawin and R. Randall, Synthesis, crystal structure, and electrochemical properties of Cu(I) coordination polymers with two new $(NS)_2$ Schiff-base ligands containing long flexible spacers, *J. Coord. Chem.*, 2013, **66**, 1974–1984.
22 D. Suresh, M. S. Balakrishna, K. Rathinasamy, D. Panda and J. T. Mague, Large-bite bis(phosphite) ligand containing mesocyclic thioether moieties: synthesis, reactivity, group 11 (CuI, AuI) metal complexes and anticancer activity studies on a human cervical cancer (HeLa) cell line, *Dalton Trans.*, 2008, 2285.
23 A. Raghuvanshi, C. Strohmann, J. B. Tissot, S. Clément, A. Mehdi, S. Richeter, L. Viau and M. Knorr, Assembly of Coordination Polymers Using Thioether-Functionalized Octasilsesquioxanes: Occurrence of (CuX)n Clusters (X = Br and I) within 3D-POSS Networks, *Chem. – Eur. J.*, 2017, **23**, 16479–16483.
24 M. Chaabéne, A. Khatyr, M. Knorr, M. Askri, Y. Rousselin and M. M. Kubicki, Bis{(4-methylthio)phenylthio}methane as assembling ligand for the construction of Cu(I) and Hg(II) coordination polymers. Crystal structures and topological (AIM) analysis of the bonding, *Inorg. Chim. Acta*, 2016, **451**, 177–186.
25 L. Jiang, Z. Wang, S. Q. Bai and T. S. A. Hor, 'Click-and-click'-hybridised 1,2,3-triazoles supported Cu(I) coordination polymers for azide–alkyne cycloaddition, *Dalton Trans.*, 2013, **42**, 9437–9443.
26 Y. Jin, H. J. Kim, J. Y. Lee, S. Y. Lee, W. J. Shim, S. H. Hong and S. S. Lee, Hard/soft heterometallic network complex of a macrocycle with endo/exocyclic coordination, *Inorg. Chem.*, 2010, **49**, 10241–10243.
27 W. J. Shi, C. X. Ruan, Z. Li, M. Li and D. Li, Tuning framework formation by flexible ligand elongation and second ligating spacer variation: Increasing dimensionality and macrocycle size, *CrystEngComm*, 2008, **10**, 778–783.
28 H. K. Tae, G. Park, W. S. Yong, K. M. Park, Y. C. Myong and J. Kim, Self-assembled copper(I) complexes of symmetric dithioether ligands, *Bull. Korean Chem. Soc.*, 2008, **29**, 499–502.
29 R. Peng, D. Li, T. Wu, X. P. Zhou and W. N. Seik, Increasing structure dimensionality of copper(I) complexes by varying the flexible thioether ligand geometry and counteranions, *Inorg. Chem.*, 2006, **45**, 4035–4046.
30 J. S. Ovens, P. R. Christensen and D. B. Leznoff, Designing Tunable White-Light Emission from an Aurophilic CuI/AuI Coordination Polymer with Thioether Ligands, *Chem. – Eur. J.*, 2016, **22**, 8234–8239.
31 P. D. Harvey and M. Knorr, Stabilization of (CuX)n Clusters (X = Cl, Br, I; n = 2, 4, 5, 6, 8) in Mono- and Dithioether-Containing Layered Coordination Polymers, *J. Cluster Sci.*, 2015, **26**, 411–459.
32 P. D. Harvey and M. Knorr, Designs of 3-Dimensional Networks and MOFs Using Mono- and Polymetallic Copper(I) Secondary Building Units and Mono- and Polythioethers: Materials Based on the Cu–S Coordination Bond, *J. Inorg. Organomet. Polym. Mater.*, 2016, **26**, 1174–1197.
33 A. Lapprand, A. Bonnot, M. Knorr, Y. Rousselin, M. M. Kubicki, D. Fortin and P. D. Harvey, Formation of an unprecedented (CuBr)5 cluster and a zeolite-type 2D-coordination polymer: a surprising halide effect, *Chem. Commun.*, 2013, **49**, 8848–8850.
34 S. Q. Liu, H. Konaka, T. Kuroda-Sowa, Y. Suenaga, H. Ito, G. L. Ning and M. Munakata, Porous copper(I) complexes of 2,11-dithia[3.3]paracyclophane: desorption and adsorption of guest molecules, *Inorg. Chim. Acta*, 2004, **357**, 3621–3631.
35 F. Juvenal, A. Langlois, A. Bonnot, D. Fortin and P. D. Harvey, Luminescent 1D- and 2D-Coordination Polymers Using CuX Salts (X = Cl, Br, I) and a Metal-Containing Dithioether Ligand, *Inorg. Chem.*, 2016, **55**, 11096–11109.
36 A. Bonnot, F. Juvenal, A. Lapprand, D. Fortin, M. Knorr and P. D. Harvey, Can a highly flexible copper(I) cluster-containing 1D and 2D coordination polymers exhibit MOF-like properties?, *Dalton Trans.*, 2016, **45**, 11413–11421.
37 A. Bonnot, P. L. Karsenti, F. Juvenal, C. Golz, C. Strohmann, D. Fortin, M. Knorr and P. D. Harvey, The 3D $[(Cu_2Br_2)\{\mu\text{-}EtS(CH_2)_4SEt\}]_n$ material: A rare example of a coordination polymer exhibiting triplet–triplet annihilation, *Phys. Chem. Chem. Phys.*, 2016, **18**, 24845–24849.
38 D. L. Dexter, A theory of sensitized luminescence in solids, *J. Chem. Phys.*, 1953, **21**, 836–850.
39 X. Li and M. L. Tang, Triplet transport in thin films: fundamentals and applications, *Chem. Commun.*, 2017, **53**, 4429–4440.
40 Q. Zhang, C. Zhang, L. Cao, Z. Wang, B. An, Z. Lin, R. Huang, Z. Zhang, C. Wang and W. Lin, Förster Energy Transport in Metal–Organic Frameworks Is Beyond Step-by-Step Hopping, *J. Am. Chem. Soc.*, 2016, **138**, 5308–5315.
41 X. Jiang, X. Guo, J. Peng, D. Zhao and Y. Ma, Triplet–Triplet Annihilation Photon Upconversion in Polymer Thin Film: Sensitizer Design, *ACS Appl. Mater. Interfaces*, 2016, **8**, 11441–11449.

42 M. Oldenburg, A. Turshatov, D. Busko, S. Wollgarten, M. Adams, N. Baroni, A. Welle, E. Redel, C. Wöll, B. S. Richards and I. A. Howard, Photon Upconversion at Crystalline Organic–Organic Heterojunctions, *Adv. Mater.*, 2016, **28**, 8477–8482.

43 T. Förster, Zwischenmolekulare Energiewanderung und Fluoreszenz, *Ann. Phys.*, 1948, **437**, 55–75.

44 A. Bonnot, M. Knorr, C. Strohmann, C. Golz, D. Fortin and P. D. Harvey, CuX (X = Cl, Br, I) Containing Coordination Polymers Built Upon Isomeric $RSCH_2C{\equiv}CCH_2SR$ (R = *p*-Tolyl, Benzyl) Dithioether Ligands: First Example of a Luminescent (CuCl)n/Dithioether Network, *J. Inorg. Organomet. Polym. Mater.*, 2015, **25**, 480–494.

45 F. R. Hartley, S. G. Murray, W. Levason, H. E. Soutter and C. A. McAuliffe, Systematics of palladium(II) and platinum(II) dithioether complexes. The effect of ligand structure upon the structure and spectra of the complexes and upon inversion at coordinated sulphur, *Inorg. Chim. Acta*, 1979, **35**, 265–277.

46 G. M. Sheldrick, A short history of SHELX, *Acta Crystallogr., Sect. A: Found. Crystallogr.*, 2008, **64**, 112–122.

47 M. J. Frisch, G. W. Trucks, H. B. Schlegel, G. E. Scuseria, M. A. Robb, J. R. Cheeseman, G. Scalmani, V. Barone, G. A. Petersson, H. Nakatsuji, X. Li, M. Caricato, A. V. Marenich, J. Bloino, B. G. Janesko, R. Gomperts, B. Mennucci, H. P. Hratchian, J. V. Ortiz, A. F. Izmaylov, J. L. Sonnenberg, D. Williams-Young, F. Ding, F. Lipparini, F. Egidi, J. Goings, B. Peng, A. Petrone, T. Henderson, D. Ranasinghe, V. G. Zakrzewski, J. Gao, N. Rega, G. Zheng, W. Liang, M. Hada, M. Ehara, K. Toyota, R. Fukuda, J. Hasegawa, M. Ishida, T. Nakajima, Y. Honda, O. Kitao, H. Nakai, T. Vreven, K. Throssell, J. A. Montgomery, Jr., J. E. Peralta, F. Ogliaro, M. J. Bearpark, J. J. Heyd, E. N. Brothers, K. N. Kudin, V. N. Staroverov, T. A. Keith, R. Kobayashi, J. Normand, K. Raghavachari, A. P. Rendell, J. C. Burant, S. S. Iyengar, J. Tomasi, M. Cossi, J. M. Millam, M. Klene, C. Adamo, R. Cammi, J. W. Ochterski, R. L. Martin, K. Morokuma, O. Farkas, J. B. Foresman and D. J. Fox, *Gaussian 16, Revision B.01*, Gaussian, Inc., Wallingford CT, 2016.

48 P. Hohenberg and W. Kohn, Inhomogeneous Electron Gas, *Phys. Rev.*, 1964, **136**, B864–B871.

49 W. Kohn and L. J. Sham, Self-Consistent Equations Including Exchange and Correlation Effects, *Phys. Rev.*, 1965, **140**, A1133–A1138.

50 R. G. Parr and W. Yang, *Density-functional theory of atoms and molecules*, Oxford University Press, 1989.

51 *The Challenge of d and f Electrons*, ed. D. R. Salahub and M. C. Zerner, American Chemical Society, Washington DC, 1989, vol. 394.

52 R. Bauernschmitt and R. Ahlrichs, Treatment of electronic excitations within the adiabatic approximation of time dependent density functional theory, *Chem. Phys. Lett.*, 1996, **256**, 454–464.

53 M. E. Casida, C. Jamorski, K. C. Casida and D. R. Salahub, Molecular excitation energies to high-lying bound states from time-dependent density-functional response theory: characterization and correction of the time-dependent local density approximation ionization threshold, *J. Chem. Phys.*, 1998, **108**, 4439–4449.

54 R. E. Stratmann, G. E. Scuseria and M. J. Frisch, An efficient implementation of time-dependent density-functional theory for the calculation of excitation energies of large molecules, *J. Chem. Phys.*, 1998, **109**, 8218–8224.

55 C. Lee, W. Yang and R. G. Parr, Development of the Colle-Salvetti correlation-energy formula into a functional of the electron density, *Phys. Rev. B: Condens. Matter Mater. Phys.*, 1988, **37**, 785–789.

56 B. Miehlich, A. Savin, H. Stoll and H. Preuss, Results obtained with the correlation energy density functionals of becke and Lee, Yang and Parr, *Chem. Phys. Lett.*, 1989, **157**, 200–206.

57 A. D. Becke, Density-functional thermochemistry. III. The role of exact exchange, *J. Chem. Phys.*, 1993, **98**, 5648–5652.

58 J. S. Binkley, J. A. Pople and W. J. Hehre, Self-consistent molecular orbital methods. 21. Small split-valence basis sets for first-row elements, *J. Am. Chem. Soc.*, 1980, **102**, 939–947.

59 M. S. Gordon, J. S. Binkley, J. A. Pople, W. J. Pietro and W. J. Hehre, Self-consistent molecular-orbital methods. 22. Small split-valence basis sets for second-row elements, *J. Am. Chem. Soc.*, 1982, **104**, 2797–2803.

60 W. J. Pietro, M. M. Francl, W. J. Hehre, D. J. DeFrees, J. A. Pople and J. S. Binkley, Self-consistent molecular orbital methods. 24. Supplemented small split-valence basis sets for second-row elements, *J. Am. Chem. Soc.*, 1982, **104**, 5039–5048.

61 K. D. Dobbs and W. J. Hehre, Molecular orbital theory of the properties of inorganic and organometallic compounds 4. Extended basis sets for third-and fourth-row, main-group elements, *J. Comput. Chem.*, 1986, **7**, 359–378.

62 K. D. Dobbs and W. J. Hehre, Molecular orbital theory of the properties of inorganic and organometallic compounds 5. Extended basis sets for first-row transition metals, *J. Comput. Chem.*, 1987, **8**, 861–879.

63 K. D. Dobbs and W. J. Hehre, Molecular orbital theory of the properties of inorganic and organometallic compounds. 6. Extended basis sets for second-row transition metals, *J. Comput. Chem.*, 1987, **8**, 880–893.

64 N. M. O'boyle, A. L. Tenderholt and K. M. Langner, cclib: A library for package-independent computational chemistry algorithms, *J. Comput. Chem.*, 2008, **29**, 839–845.

65 A. Raghuvanshi, M. Knorr, L. Knauer, C. Strohmann, S. Boullanger, V. Moutarlier and L. Viau, 1,3-Dithianes as Assembling Ligands for the Construction of Copper(I) Coordination Polymers. Investigation of the Impact of the $RC(H)S_2C_3H_6$ Substituent and Reaction Conditions on the Architecture of the 0D–3D Networks, *Inorg. Chem.*, 2019, **58**, 5753–5775.

66 P. D. Harvey and M. Knorr, Stabilization of $(CuX)_n$ Clusters (X = Cl, Br, I; n = 2, 4, 5, 6, 8) in Mono- and Dithioether-Containing Layered Coordination Polymers, *J. Cluster Sci.*, 2015, **26**, 411–459.

67 P. D. Harvey and M. Knorr, Designs of 3-Dimensional Networks and MOFs Using Mono- and Polymetallic Copper(I) Secondary Building Units and Mono- and Polythioethers: Materials Based on the Cu–S Coordination Bond, *J. Inorg. Organomet. Polym. Mater.*, 2016, **26**, 1174–1197.

68 M. Knorr, A. Khatyr, A. Dini Aleo, A. El Yaagoubi, C. Strohmann, M. M. Kubicki, Y. Rousselin, S. M. Aly, D. Fortin, A. Lapprand and P. D. Harvey, Copper(I) halides (X = Br, I) coordinated to bis(arylthio)methane ligands: aryl substitution and halide effects on the dimensionality, cluster size, and luminescence properties of the coordination polymers, *Cryst. Growth Des.*, 2014, **14**, 5373–5387.

69 A. Bonnot, M. Knorr, F. Guyon, M. M. Kubicki, Y. Rousselin, C. Strohmann, D. Fortin and P. D. Harvey, 1,4-Bis-(arylthio)but-2-enes as Assembling Ligands for $(Cu_2X_2)_n$ (X = I, Br; n = 1, 2) Coordination Polymers: Aryl Substitution, Olefin Configuration, and Halide Effects on the Dimensionality, Cluster Size, and Luminescence Properties, *Cryst. Growth Des.*, 2016, **16**, 774–788.

70 A. Schlachter, L. Viau, D. Fortin, L. Knauer, C. Strohmann, M. Knorr and P. D. Harvey, Control of Structures and Emission Properties of $(CuI)_n$ 2-Methyldithiane Coordination Polymers, *Inorg. Chem.*, 2018, **57**, 13564–13576.

71 M. Knorr, F. Guyon, A. Khatyr, C. Strohmann, M. Allain, S. M. Aly, A. Lapprand, D. Fortin and P. D. Harvey, Construction of $(CuX)_{2n}$ cluster-containing (X = Br, I; N = 1, 2) coordination polymers assembled by dithioethers $ArS(CH_2)$ mSAr (Ar = Ph, *p*-Tol; M = 3, 5): Effect of the spacer length, aryl group, and metal-to-ligand ratio on the dimensionality, cluster, *Inorg. Chem.*, 2012, **51**, 9917–9934.

72 P. D. Harvey, *The Porphyrin Handbook: Multporphyrins, Multiphthalocyanines and Arrays*, Elsevier, 2012, vol. 18, pp. 63–250.

73 M. Adams, M. Kozlowska, N. Baroni, M. Oldenburg, R. Ma, D. Busko, A. Turshatov, G. Emandi, M. O. Senge, R. Haldar, C. Wöll, G. U. Nienhaus, B. S. Richards and I. A. Howard, Highly Efficient One-Dimensional Triplet Exciton Transport in a Palladium–Porphyrin-Based Surface-Anchored Metal–Organic Framework, *ACS Appl. Mater. Interfaces*, 2019, **11**, 15688–15697.

74 H. Miyasaka and N. Mataga, Temperature Dependence of Singlet Excitation Energy Migration in Liquid Benzene as Revealed by Picosecond Laser Photolysis, *Stud. Phys. Theor. Chem.*, 1995, **83**, 393–396.

75 S. Faure, C. Stern, R. Guilard and P. D. Harvey, Role of the Spacer in the Singlet–Singlet Energy Transfer Mechanism (Förster *vs.* Dexter) in Cofacial Bisporphyrins, *J. Am. Chem. Soc.*, 2004, **126**, 1253–1261.